Supporting Materials

Quantifying and modeling of stress-driven short-circuit in lithium-ion batteries in electrified vehicles

Binghe Liu [a*], Xudong Duan [b, c*], Chunhao Yuan [d, e], Lubing Wang [f, g], Jiani Li [d, e], Donal P. Finegan [h], Bill Feng [i], Jun Xu [d, e†]

[a]*School of Automotive Engineering, Chongqing University, Chongqing 400044, China* [b]*Vehicle Energy & Safety Laboratory (VESL), Beihang University, Beijing, China, 100191*

[c]*Department of Automotive Engineering, School of Transportation Science and Engineering, Beihang University, Beijing 100191, China*

[d]*Department of Mechanical Engineering and Engineering Science, The University of North Carolina at Charlotte, Charlotte, NC 28223, USA.*

[e]*Vehicle Energy & Safety Laboratory (VESL), North Carolina Motorsports and Automotive Research Center, The University of North Carolina at Charlotte, Charlotte, NC 28223, USA.*

[f]*Safety Engineering, Ministry of Education, Ningbo University, Ningbo 315211, China*

[g]*Department of Mechanics and Engineering Science, Faculty of Mechanical Engineering & Mechanics, Ningbo University, Ningbo 315211, China*

[h]*National Renewable Energy Laboratory, 15013 Denver West Parkway, Golden CO 80401, USA*

[i]*Jaguar Land Rover, Coventry, CV34LF, UK*

---

[*]These authors contributed equally.
[†]Corresponding author: Prof. Jun Xu at jun.xu@uncc.edu; Tel: (704)-687-8240; Fax: (704)-687-8240

To better observe the cracks of the current collector, the coatings were removed. The removing methods for each component are illustrated in Fig. S1.
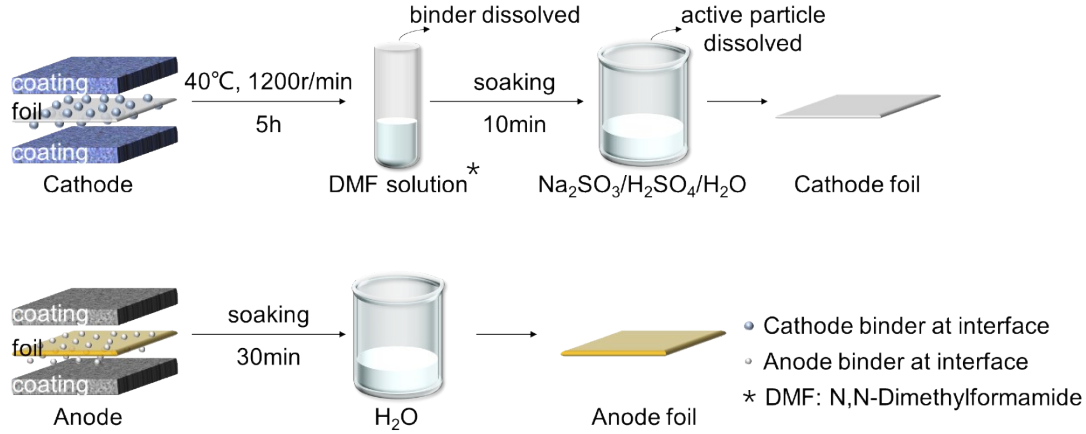
Fig.S1 The process of removing coatings of electrodes.

The Electrochemical Impedance Spectroscopy (EIS) in each compression displacement shows, the impedance of the battery started to increase after 4.7 mm (Fig. S2), which is supporting evidence of minor ISCs [1].
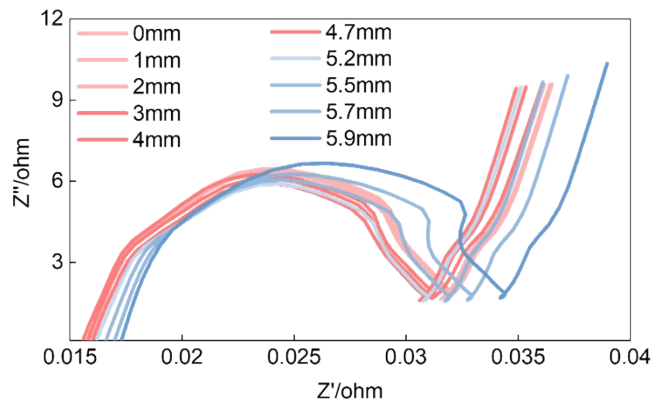
Fig. S2 EIS experiment results at different compression displacements.

To reveal the mechanism of the temperature response during the whole compressive process (Fig. 4(a)), we use the energy balance equation to estimate the temperature rise at key points :

$$\rho C_p \frac{\partial T}{\partial t} + \nabla \cdot \boldsymbol{q} = Q_s \qquad (1)$$

where ρ is the mass density of jellyroll, C_p is the specific heat capacity of jellyroll, T is temperature, q is the heat flux and Q_s represents the total volumetric heat sources, which consist of the following heat sources:

$$Q_s = Q_{bat} + Q_{ISC} + Q_{tr} \tag{2}$$

where Q_{bat} is the battery heat induced by electrochemical reactions, Q_{ISC} is the ISC heat (joule heat) induced by ISC current and resistance related to the mechanical behaviors of each component in the battery, and Q_{tr} is the heat from the thermal runaway. The thermal runaway heat is often considered as the sum of the heat production from four chemical reactions induced when the temperature reaches 90 °C, including SEI decomposition, anode-electrolyte reaction, cathode-electrolyte reaction, and electrolyte decomposition. Note that the area of temperature rise captured by the infrared thermal imager locates in the jellyroll, so only the thermal parameters of the jellyroll are needed. Since the temperature distribution of each moment can be recorded and the time interval of temperature rise was observed to be very short, the heat flux and the battery heat are neglected when the temperature rise is estimated. Then the equation is simplified as:

$$\rho C_p \frac{\Delta T}{\Delta t} = Q_{ISC} + Q_{tr} \tag{3}$$

where ΔT is the temperature rise during the time interval Δt.

At Point 1 (Fig. 4(a)), the minor ISC has happened and ISC heat Q_{ISC}^{minor} can be calculated by :

$$Q_{ISC}^{minor} = \frac{I_1^2 R_{minor}}{V_{minor}} \tag{4}$$

$$I_1 = \frac{U}{R_{minor}} \tag{5}$$

$$V_{minor} = \frac{R_{minor}}{100\Omega \cdot mm^2} \times h_{jell} \qquad (6)$$

where U is the initial open circuit voltage (OCV) and h_{jell} is the thickness of one layer of jellyroll.

V_{minor} represents the zone where minor ISC happens. According to the filming frequency of 30 frames in one second of the Thermal Camera, the time interval can be decided $\Delta t_1 = 0.033s$. During this time, the chemical reactions related to thermal runaway can be neglected $Q_{tr} = 0$ due to the temperature far below 90 ℃. Other needed parameters are summarized in Table S1. Then temperature rise ΔT_1 where minor ISC happens can be calculated.

At Point 6 (Fig. 4(a)), the major ISC has happened and the resistance R_{major} can be estimated by :

$$\Delta U = \frac{U \times R_{inter}}{R_{inter} + R_{major}} \qquad (7)$$

where R_{inter} is the internal resistance of the battery. Previous researches have proposed that ISC heat is much higher than thermal runaway heat when the batteries are in low SOC (SOC of the samples used in our tests are all 0.1). Herein, the thermal runaway heat can also be neglected $Q_{tr} = 0$. Similarly, Q_{ISC}^{major} can be calculated by :

$$Q_{ISC}^{major} = \frac{I_2^2 R_{major}}{V_{major}} \qquad (8)$$

$$I_2 = \frac{U}{R_{major}} \qquad (9)$$

where V_{major} is estimated through the image captured by the Thermal Camera at Point 6 and the measurement of damage area after disassembling. Then the temperature rise at Point 6 ΔT_2 can be calculated.

Table S1. The parameters used for calculation of temperature rise during compression.

Parameters	Value	References
ρ	2.247e3 kg/m^3	2
C_p	785 J/(kg · K)	2
U	3.3758 V	measured
h_{jell}	0.252 mm	measured
R_{inter}	0.048Ω	provided
V_{major}	6.98mm^3	estimated

The minor ISC was identified by the continuous drop of dU/dt. There are three steps to identify the minor ISC triggering point.

Step 1: Extract the data for analysis. Extract the data before the voltage drop 0.01V abruptly.

Step 2: Choose the zones to be identified. Zones where the range of $\mathrm{d}^2 U / \mathrm{d}t^2 < 0$ exceeds 0.2 mm (2s) are regarded as the "suspicious" zones of minor ISC triggering zone to be further identified.

Step 3: Identify the minor ISC triggering point. First, select the dU/dt data within the initial 0.2mm range of each suspicious curve for a linear fitting and calculate the standard deviation, Σ. The linear fitting curve serves as the baseline, and two boundaries can be confirmed based on the three-sigma rule. This zone represents that almost all subsequent dU/dt data should be in this region, and if the actual dU/dt data exceeds this range, there must be some factors leading to the change of internal battery state. If the follow-up dU/dt curve is higher than the region, it is considered that the curve is no longer dropping, and the minor ISC is not triggered. Otherwise, it is considered that the irreversible change is caused by the minor ISC, and the starting point of the

suspicious region is regarded as the trigger point of the minor ISC.

The minor ISC identified method is then used in all loading conditions, and Fig. S3(a) shows the example of the compression loadings. The indentified results for the other loading conditions are shown in Figs. S3(b)-(d).
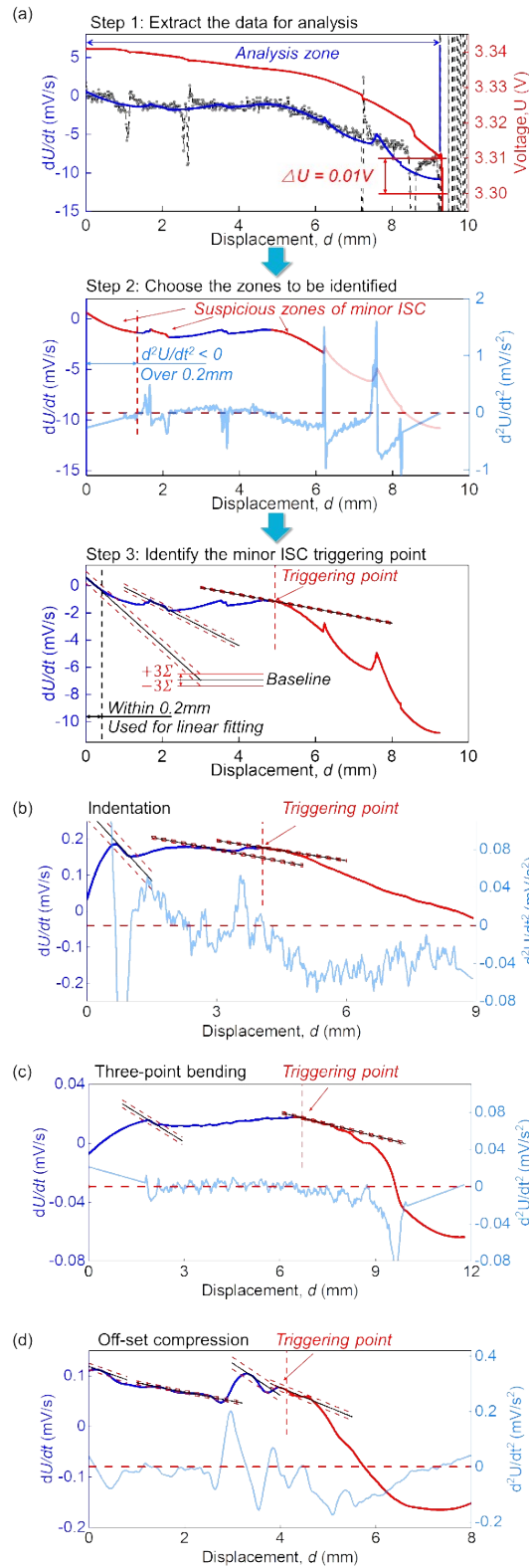
Fig. S3 (a) A demonstration case to identify the minor ISC triggering point for compression loadings, and the indentified results for (b) indentation, (c) bending and (d) offset compression.

Given the complicated multiphysics nature of LIBs, we used the method proposed in our previous study[38] and established a multiphysics to describe the process for the LIB subjected to compressive loading. With the increase of compression displacement, stress concentration firstly appeared at the center of the section, and when it reached Point 1, maximum equivalent plastic strain (PEEQ) was just over 0.2755 (Fig. 6(c)), which was set to the critical PEEQ value of minor ISC, $\bar{\varepsilon}^*_{eq,minor} = 0.2775$. The model summed up the area where the strain exceeded $\bar{\varepsilon}^*_{eq,minor}$ and obtained the minor ISC area, S_{mt} which was further normalized as follows:

$$S^*_{mt} = \frac{S_{mt}}{\pi R^{LB^2}} \qquad (10)$$

where R^{LB} is the radius of LIB. The compression displacement increased continuously and the minor ISC area expanded, leading to the decrease of minor ISC resistance R_{minor}. The relationship between stress/strain and R_{minor} was described as follows:

$$R_{minor} = R^{initial}_{minor}(1\text{-}S^*_{minor}) \qquad (11)$$

where $R^{initial}_{minor}$ is a fitting parameter. By comparing experiment and simulation results, the value of $R^{initial}_{minor}$ was confirmed as 200Ω.

Similarly, the PEEQ value of major ISC was set as $\bar{\varepsilon}^*_{eq,major} = 0.351$ (Fig. 6(d)) and the major ISC resistance R_{major} was set as $R_{major} = R^{initial}_{major}(1\text{-}S^*_{major})$, where $R^{initial}_{major}$ was confirmed as 0.1Ω and S^*_{major} was normalized from the major ISC area. More details to establish the Multiphysics model can be found in Ref. [38].

Figs.6(c) and (d) show that the model can predict both the dU/dt-time   and the voltage-time curves

decently and the temperature distribution predicted by the model can match with the test results shown in Fig.4(c). From the model, we confirmed some conclusions:

- Stress/strain is the most direct causation of ISCs and the stress/strain concentration determines the location of ISCs;

- At Point 1, minor ISC was triggered and a minor ISC resistance about 200Ω was induced;

- With the increase of compression loading, the minor ISC region continued tol expand and lead to the decrease of minor ISC resistance;

- At Point 5, a much more serious ISC occurred with a ISC resistance of 0.1Ω in the area of stress/strain concentration leading to the temperature concentration.

All the battery samples used to explore the ISC mechanism were charged to 0.1 SOC and tested at the room temperature. It needs to be pointed that the SOC and environmental temperature can impact the ISC behavior under various loading conditions. Ref. [3] has reported that lower environmental temperature would soften the battery and made it easier to be crushed. Our previous studies [4, 5] have explored the relationship between mechanical parameters and SOC, and proposed some functions with SOC as the independent variable to describe the mechanical parameters, including the structural stiffness, nominal failure stress, and strain. Herein, we additionaly conducted compression, indentation, and three-point bending tests using complete LIB cells (without removing the negative cap) with different SOC values, and the results are summarized in Fig. S4. It shows that the mechanical and ISC behaviors have SOC dependency, which has a good agreement with our previous study32. With the increase of SOC, the moment of minor ISC was closer and closer to that of major ISC, and the range of dU/dt became smaller. For further study,

we can combine the EIS and disassembly experiments to identify minor ISC precisely and use the method in Ref. [4] to establish the functions between the mechanical parameters & critical values of ISCs and the variable of SOC.
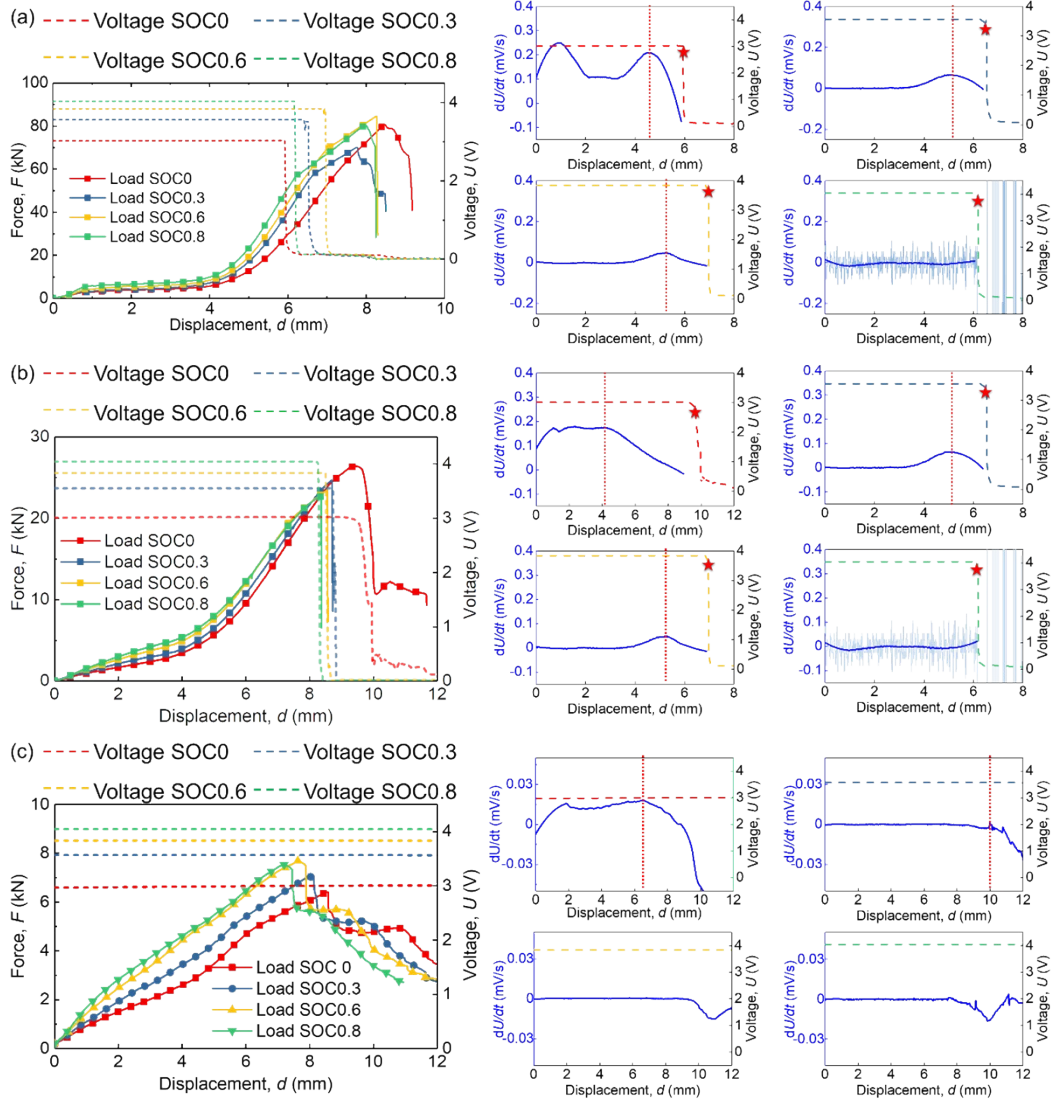
Fig. S4 The force-, voltage-, dU/dt-displacement curves and the markers of minor/major ISCs from experiments using LIBs with different SOCs (the red dotted line represents the minor ISC and the red star point represents major ISC) under (a) compression (LIBs without removing the negative cap), (b) Indentation and (c) Three-point bending

To build the finite element model of the battery (the geometric configuration of the cross

section is shown in Fig. S4(a)) which can predict the mechanical deformation of the whole structure and the failure of the local components, both the equivalent model (the composing of 1 layer of the anode, 1 layer of the cathode, and 2 layers of the separator is regarded as one homogenized material with equivalent material properties) and detailed model (considering the detail of the layers) are used, as shown in Fig. S4(b).
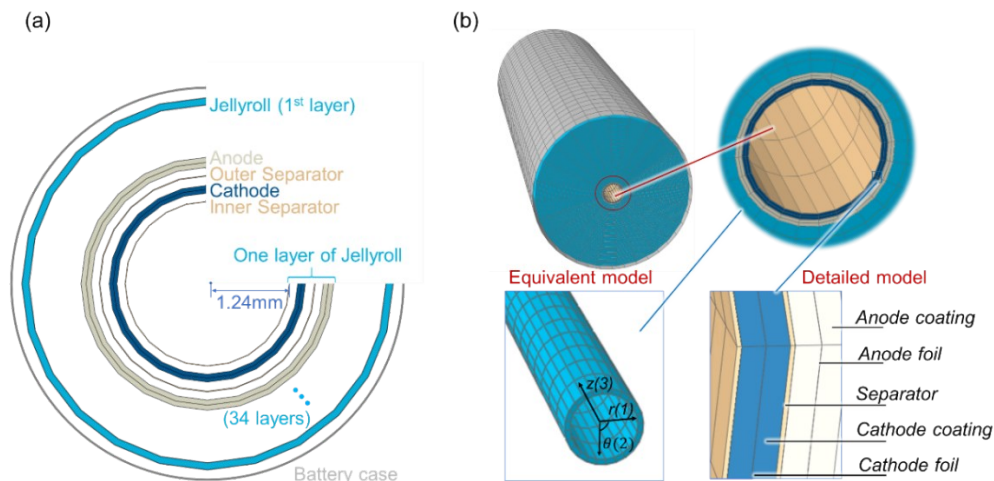
Fig. S5 The schematic diagram of the target battery, (a) geometric configuration of cross-section, (b) the equivalent model, and a detailed model of LIB.

The experiments for the components included *in-situ*/*ex-situ* characterization experiments in tension, compression, and indentation. For the cell level, compression, indentation, bending, and offset compression were conducted. Thermal field, load, and voltage were measured for compression loadings (the cap of the battery is removed in this loading), and the load and voltage are measured in the other three loadings
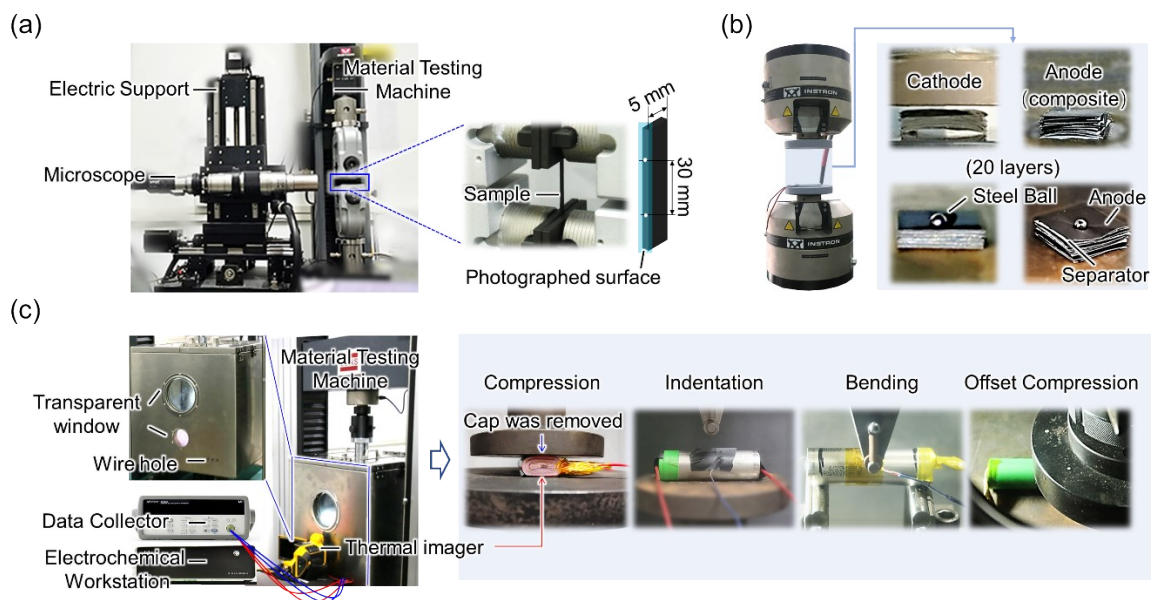
Fig. S6 (a) the in-situ experiment setting for tension, (b) the experiment settings for stacking compression and indentation, and (c) the experiment settings for LIB under different loading conditions.

The failures of the repeated experiments for the components on compression and indentation are summarized in Fig. S7.

Loading condition	Material	Test number	Results	
			Force level 1	Force level 2
compression	cathode	Test 1		
		Test 2		
	anode (composite)		3rd Layer-foil & separator	
		Test 1		
		Test 2		
Indentation	cathode		1st Layer-Foil	1st Layer-Foil 4th Layer-Foil
		Test 1		
		Test 2		
	anode (composite)		1st Layer-foil & separator	5th Layer-foil & separator
		Test 1		
		Test 2		
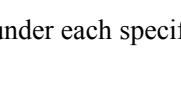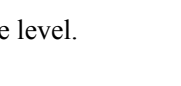
Fig. S7 The morphology of samples under each specific force level.

The *ex-situ* characterization was conducted in different force levels. The chosen of the force levels in compression and indentation loadings are summarized in Table S2.

Table S2. The preset force levels and examination method of samples in compression and indentation tests.

Loading condition	Material	Force level (kN)	Sample preparation
Compression	cathode	80, 100	/
	anode (composite)	20,60	Remove coating
Indentation	cathode	0.4, 0.8	Remove coating
	anode (composite)	0.4, 0.7	Remove coating + microscope

The geometric parameters of the components of the LIB is summarized in Table S3.

Table S3. Geometric parameters of components.

Components	Thickness (mm)	Length (mm)	Neutral zone radius (mm)
Battery case	0.2	70.3	10.65
Jellyroll	0.252		10.186 (outermost layer)
Cathode-foil	0.01		/
Cathode-coating	0.05		/
Anode-foil	0.02	65	/
Anode-coating	0.05		/
Separator	0.011		/

* The lengths of electrodes and separators are considered to be the same as that of the jellyroll.

The mechanical mesh parameters of the components for the tensile FEM and other loading conditions are summarized in Table S4 and S5 separately.

Table S4. Mechanical and mesh parameters of components for tensile FEM.

Components	Modulus (MPa)	Poisson ratio	Yield stress (MPa)	Damage initiation strain	Damage evolution	Interfacial adhesive strength (kPa)	Global mesh size (mm)
Cathode-foil	25470.7		80.79	0.0147	0		0.02
Cathode-coating	4513.22		10.23	0.14	0	/	0.02
Anode-foil	28000	0.3	70	0.2	0.001		0.02
Anode-coating	4510		16.64	0.065	0.002	248 [22]	0.02
Separator	1160		14.201	0.3	0	/	0.25

Table S5. Mechanical and mesh parameters of components for all loading conditions.

Components	Modulus (MPa)			Poisson ratio			Shear modulus (MPa)			Plastic parameters			Damage initiation strain	Damage evolution	Mesh size (mm)	Element number
	E_1	E_2	E_3	v_1	v_2	v_3	G_{12}	G_{13}	G_{23}	Yield stress (MPa)	Crushable foam k	k_t				
Battery case		211000			0.3			/		358.7	/	/	/	/	0.74-2.33	1480/1340(without cap)
Jellyroll	700	6929	6929	0.15	0.15	0.3	1017	1017	2665	0.56	/	/	/	/	0.25-2.69	25920 (36 circles in total)
Cathode-foil		70623.9			0.3			/		154.614	/	/	0.5	0.01	0.25*	/
Cathode-coating		4000			0			/		/	2.3	0.05	0.22	0.135	0.25*	/
Anode-foil		45425.1			0.3			/		161.039	/	/	0.4	0.01	0.5*	/
Anode-coating		700			0.3			/		/	2	0.4	0.5	0.12	0.5*	/
Separator		1160			0.3			/		14.201	/	/	0.3	0	0.5*	/

* The presentative mesh size of each component used in compression models

Reference

1. X. Kong, G. L. Plett, M. S. Trimboli, Z. Zhang, D. Qiao, T. Zhao and Y. Zheng, *Journal of Energy Storage*, 2020, **27**, 101085.
2. C. H. Yuan, X. Gao, H. K. Wong, B. Feng and J. Xu, *J. Electrochem. Soc.*, 2019, **166**, A1160-A1169.
3. Z. Gao, X. Zhang, Y. Xiao, H. Gao, H. Wang and C. Piao, *Energies*, 2019, **12**.
4. J. Xu, B. Liu and D. Hu, *Sci Rep-UK*, 2016, **6**, 21829.
5. L. Wang, S. Yin, C. Zhang, Y. Huan and J. Xu, *J. Power Sources*, 2018, **392**, 265-273.